



# Catalyst-assisted chemical looping for CO<sub>2</sub> conversion to CO



Vladimir V. Galvita<sup>a,\*</sup>, Hilde Poelman<sup>a</sup>, Christophe Detavernier<sup>b</sup>, Guy B. Marin<sup>a</sup>

<sup>a</sup> Laboratory for Chemical Technology, Ghent University, Technologiepark 914, B-9052 Ghent, Belgium

<sup>b</sup> Department of Solid State Sciences, Ghent University, Krijgslaan 281, S1, B-9000 Ghent, Belgium

## ARTICLE INFO

### Article history:

Received 8 July 2014

Received in revised form 3 September 2014

Accepted 7 September 2014

Available online 16 September 2014

### Keywords:

Dry reforming

FeNi<sub>3</sub> alloy

Fe<sub>2</sub>O<sub>3</sub>–CeO<sub>2</sub>

Surface carbon conversion

## ABSTRACT

A bifunctional 5% Ni/CeO<sub>2</sub>–Fe<sub>2</sub>O<sub>3</sub> (1:1) sample was prepared for the transformation of CO<sub>2</sub> to CO by catalyst-assisted chemical looping. Generation of CO from CO<sub>2</sub> through CH<sub>4</sub> + CO<sub>2</sub>/CO<sub>2</sub> redox cycles was investigated between 873 K and 973 K. In the reduction step, CH<sub>4</sub> + CO<sub>2</sub> is converted over Ni into syngas, which then reduces the CeO<sub>2</sub>–Fe<sub>2</sub>O<sub>3</sub> oxygen storage material, yielding CO<sub>2</sub> and H<sub>2</sub>O. CO is produced upon re-oxidation of the oxygen storage material by CO<sub>2</sub>. The addition of Ni to CeO<sub>2</sub>–Fe<sub>2</sub>O<sub>3</sub> has a beneficial effect upon the activity of the material during periodic cycling. The crystallographic structure of the sample was examined using time-resolved in situ X-ray diffraction under H<sub>2</sub> reduction and CO<sub>2</sub> oxidation. H<sub>2</sub>-TPR reduced the Fe<sub>2</sub>O<sub>3</sub> phase to Fe<sub>3</sub>O<sub>4</sub>, FeO and Fe. From 600 K onwards NiO reduction is initiated. Interaction between Ni and Fe leads to Ni<sub>3</sub>Fe alloy formation from 850 K onwards. This alloy remains stable up to 873 K during CO<sub>2</sub> re-oxidation but is completely decomposed into Ni and Fe<sub>3</sub>O<sub>4</sub> at 973 K. This re-oxidation of iron follows a one-step pathway to Fe<sub>3</sub>O<sub>4</sub> between 773 K and 873 K, but a two-step pathway above 873 K. The methane reforming on the Ni-based catalyst is accompanied with formation and accumulation of surface carbon. This carbon is removed by oxidation with lattice oxygen from CeO<sub>2</sub>–Fe<sub>3</sub>O<sub>4</sub> during or after re-oxidation with CO<sub>2</sub>.

© 2014 Elsevier B.V. All rights reserved.

## 1. Introduction

Fossil fuels are the world's major source of energy and have a great impact on human prosperity [1,2]. Considering the depletion of fossil fuels due to continuously increasing energy demand, there is a need to investigate ways to more efficiently utilize available resources including natural gas reserves. Apart from natural gas reserves, biogas produced from anaerobic decomposition of organic material is also a source of gas with nearly equal concentrations of CH<sub>4</sub> and CO<sub>2</sub> [3,4]. Among the most widely studied technologies for conversion of CH<sub>4</sub> to mixtures of H<sub>2</sub> and CO are various reforming techniques such as steam reforming, dry reforming, partial oxidation and autothermal reforming [5,6]. These techniques differ in the oxidant used, the final H<sub>2</sub>/CO product ratio and the kinetics and energetics of the reaction. Dry reforming in particular utilizes two abundantly available green-house gases CH<sub>4</sub> and CO<sub>2</sub>, to produce the industrially important syngas H<sub>2</sub> + CO [6]. The overall activity of a catalyst used for dry reforming depends on the type of metal used, the nature of the support, its surface area, the metal particle size and the interaction between metal

and support. Noble metals such as Pt, Rh and Ru are highly active towards dry reforming and are more resistant to carbon formation than other transition metals, but are expensive.

As an alternative to conventional technologies, methane reforming based on chemical looping is a process which was designed to convert hydrocarbons to hydrogen and/or carbon monoxide [7–19]. The technology is based on periodic reduction/re-oxidation cycling of metal oxides. During the first step, methane (or gasified biomass) reduces the metal oxide to metal and produces CO<sub>2</sub> and H<sub>2</sub>O (Eq. (1)). In the second step, carbon dioxide is used as an oxidizing agent, simultaneously producing carbon monoxide according to Eq. (2).



By summing up the Eqs. (1) and (2), one obtains the overall reaction which is the endothermic carbon dioxide reforming of methane into CO:



According to Eq. (2), 1 kg of iron can transform 0.54 Nm<sup>3</sup> of CO<sub>2</sub> per reduction and oxidation cycle. The overall process utilizes more carbon dioxide than it produces in the reduction step. In the case of CH<sub>4</sub>, the process can convert three times as much CO<sub>2</sub> than is produced. This process can be made even more efficient if the

\* Corresponding author. Tel.: +32 93311722

E-mail address: [vladimir.galvita@UGent.be](mailto:vladimir.galvita@UGent.be) (V.V. Galvita).

reactor can be heated using solar energy as external heat source. This carbon dioxide–methane reforming differs significantly from conventional catalytic dry reforming processes. The target of conventional dry reforming is high syngas yield. However, the present chemical looping process is designed with the goal of maximum CO yield.

The chemical looping conversion of CO<sub>2</sub> into CO over an oxygen storage material is one of the possible technologies for CO<sub>2</sub> utilization. The ability of the oxygen storage material to maintain its high activity in repeated reduction/re-oxidation cycles is the most critical issue for the CO<sub>2</sub> splitting process. Among the possible materials, Fe<sub>2</sub>O<sub>3</sub>–CeO<sub>2</sub> stands out because of its high activity in both reduction and CO<sub>2</sub> re-oxidation. The addition of CeO<sub>2</sub> to Fe<sub>2</sub>O<sub>3</sub> has proven to have a beneficial effect upon the activity and stability of the material [13]. Reduction–re-oxidation cycles can be repeated many times without significant loss of CO<sub>2</sub> conversion efficiency. The highest CO yield was obtained for 20 wt% CeO<sub>2</sub> in Fe<sub>2</sub>O<sub>3</sub> while 70 and 50 wt% CeO<sub>2</sub>–Fe<sub>2</sub>O<sub>3</sub> were the most stable combinations [13].

The typical challenges for current dry reforming technologies are catalyst cost and their deactivation due to coking, as well as product selectivity. However, the chemical looping dry reforming (CLDR) process differs significantly from conventional catalytic dry reforming processes. While the target of conventional dry reforming is high syngas yield, CLDR is now optimized for CO<sub>2</sub> activation. Therefore, CLDR can also be conceptualized as a process that concentrates dilute streams of CO<sub>2</sub> [16,20]. By utilizing CLDR, the carbon dioxide emitted by power plants and industrial units could be utilized and industrial users would not need to establish new subsidiary units for the treatment of carbon dioxide. A proof of principle of the CLDR concept was described in Ref. [13,20].

CO production by the chemical looping process is limited by the slower step, which is the reduction of Fe<sub>3</sub>O<sub>4</sub> by methane in the presence of CO<sub>2</sub>. The natural mixture of methane with carbon dioxide (biogas CO<sub>2</sub>/CH<sub>4</sub> > 1) significantly decreases the reduction rate of iron oxide [10,21,22] because carbon dioxide also acts as an oxidizing agent [10,23]. Both CO<sub>2</sub> in the feed and product CO<sub>2</sub> have this effect on the iron oxide reduction rate. In order to overcome this limitation, a physical mixture of a Ni-based catalyst and iron oxide as an oxygen storage material can be used [24]. During the first step, a mixed feed of CH<sub>4</sub> and CO<sub>2</sub> over Ni/Al<sub>2</sub>O<sub>3</sub> is converted to syngas (Eq. (4)):



Both CO and H<sub>2</sub> then reduce the iron oxide:



The reduction of iron oxide by H<sub>2</sub> and CO is considerably faster than by only methane [7,17].

The catalysts that are employed in the dry reforming process range from noble metals (Rh, Ru, Pt, Pd, Ir) to base metals (Ni, Co) supported over metal oxides, mixed oxides and perovskites. Particular attention has been devoted to the development of non-noble metal catalysts, due to high cost and limited availability of noble metals. Nickel-based catalysts are among the most investigated catalytic systems, despite their rapid deactivation by coking. Redox support materials, such as ceria-based solid solutions or mixed oxides to disperse the active Ni content, are generally employed to mitigate catalyst deactivation by carbon deposition. High dispersion of Ni is important for active and stable catalysts in methane dry reforming [25–27]. CeO<sub>2</sub>, in particular, is widely used as a promoter since it increases Ni dispersion and with its redox couple (Ce<sup>4+</sup>/Ce<sup>3+</sup>), CeO<sub>2</sub> easily gasifies surface deposited coke by storing and delivering active oxygen [28]. Daza et al. (2009) [29] have reported that the catalytic activity of a Ni–Ce/mineral clay catalyst

was enhanced and coke formation was restricted in dry reforming of methane due to improved Ni dispersion and CO<sub>2</sub> adsorption. Potdar et al. (2002) [30] have reported that a Ni–Ce nanocatalyst showed a stable reaction activity and coke resistance due to its high surface area and high oxygen mobility in the carbon dioxide reforming process. The modification of Ni with Fe has been attempted because Fe can interact with Ni by the formation of a Ni–Fe alloy and Fe species have high redox capacity, much like Ce species [31]. Nickel–iron mixed oxides were tested in steam reforming of ethanol for hydrogen production [32]. Nickel–iron oxide (NiFe<sub>2</sub>O<sub>4</sub>) has been tested as a combined catalyst precursor and oxygen transfer material for improved conversion of methane in steam reforming [33]. Iron–alumina-supported nickel–iron alloy catalysts were explored for steam reforming of toluene as a biomass tar model compound. The catalyst exhibited the best steam reforming performance in terms of higher catalytic activity and stability [34].

The objective of the present study is the design of a novel bifunctional material for the catalyst-assisted chemical looping process by combining two aforementioned strategies: catalytic conversion of CH<sub>4</sub> and CO<sub>2</sub> to syngas over a Ni-based catalyst, and enhanced oxygen storage in a mixed oxide CeO<sub>2</sub>–Fe<sub>2</sub>O<sub>3</sub>. Catalyst-assisted chemical looping was investigated using a Ni/CeO<sub>2</sub>–Fe<sub>2</sub>O<sub>3</sub> sample for the transformation of CO<sub>2</sub> to CO. CeO<sub>2</sub>–Fe<sub>2</sub>O<sub>3</sub> acts both as a support for Ni as well as an oxygen storage material for the chemical looping process. Experimental performance data as well as structural characterization of the bifunctional material reduction and CO<sub>2</sub> re-oxidation are reported herein.

## 2. Experimental

### 2.1. Materials preparation

Samples of 5 wt% Ni/CeO<sub>2</sub>–Fe<sub>2</sub>O<sub>3</sub> were investigated in this study. The following chemicals were used in the preparation of the mixed oxides: Fe(NO<sub>3</sub>)<sub>3</sub>·9H<sub>2</sub>O (99.99+%, Sigma-Aldrich), and Ce(NO<sub>3</sub>)<sub>3</sub>·6H<sub>2</sub>O (99.99%, Sigma-Aldrich). CeO<sub>2</sub>–Fe<sub>2</sub>O<sub>3</sub> was prepared in a 1:1 ratio by co-precipitation through addition of excess ammonium hydroxide. This mixture was maintained at room temperature for 12 h. Next, the sample was separated as precipitate from the solution, washed with water and dried overnight in an oven at 383 K. Finally, the materials were calcined at 1023 K.

The resulting 5 wt% Ni/CeO<sub>2</sub>–Fe<sub>2</sub>O<sub>3</sub> catalyst, labelled as Ni/Ce–Fe, was prepared by incipient wetness impregnation using a solution containing the required amount of nickel nitrate salt, Ni(NO<sub>3</sub>)<sub>2</sub>·2H<sub>2</sub>O (99.99%, Sigma-Aldrich). The prepared catalyst was dried overnight in an oven at 383 K and calcined at 1023 K.

### 2.2. General characterization

The Brunauer–Emmett–Teller (BET) surface area of each sample was determined by N<sub>2</sub> adsorption at 77 K (five point BET method using Gemini Micromeritics). Prior to analysis sample was outgassed at 300 °C for 6 h to eliminate volatile adsorbates from the surface. Pure 50%CeO<sub>2</sub>–50%Fe<sub>2</sub>O<sub>3</sub> (Ce–Fe) and 5%Ni–50%CeO<sub>2</sub>–50%Fe<sub>2</sub>O<sub>3</sub> (Ni/Ce–Fe) have a similar BET surface area (~15 m<sup>2</sup>/g).

The crystallographic phase of the prepared materials was determined using a Siemens Diffractometer Kristalloflex D5000, with Cu K $\alpha$  radiation. The powder XRD patterns were collected in a 2 $\theta$  range from 10° to 80° with a step of 0.02° and 30 s counting time per angle. By fitting a Gaussian function to a diffraction peak, the crystallite size can be determined from the peak width via the Scherrer equation [35] while the peak position gives information about the lattice spacing based on the Bragg's law of diffraction:  $2d\sin(\theta) = n\lambda$  [36].

For Ni/Ce–Fe only  $\text{Fe}_2\text{O}_3$ ,  $\text{CeO}_2$  and NiO diffractions were observed. The peaks of NiO (2 0 0),  $\text{CeO}_2$  (1 1 1) and  $\text{Fe}_2\text{O}_3$  (1 1 0) were used to determine the crystallite size, yielding  $15 \pm 7$  nm for NiO,  $50 \pm 5$  nm for  $\text{Fe}_2\text{O}_3$  and  $20 \pm 10$  nm for  $\text{CeO}_2$ . The latter values are in line with previous work on a series of  $\text{Fe}_2\text{O}_3$ – $\text{CeO}_2$ , where the mixing was proven to reduce particle sizes, thus diluting both compounds [13].

Morphological, structural and local chemical analyses were carried out using transmission electron microscopy (TEM)-based methods: conventional TEM, high resolution (HRTEM), scanning transmission bright field (STEM BF) and energy dispersive X-ray spectrometry (EDX). The instrument employed in this study was a JEOL JEM-2200FS: Cs-corrected, operated at 200 kV, and equipped with a Schottky-type field-emission gun (FEG), EDX JEOL JED-2300D and JEOL in-column omega filter (EELS). Specimens were prepared by immersion of a lacey carbon film on a copper support grid into the as prepared powder followed by blowing off the excess powder. Particles sticking to the carbon film were subjected to microscopy. A beryllium specimen retainer was used to eliminate secondary X-ray fluorescence in EDX spectra originating from the specimen holder.

### 2.3. In situ time-resolved XRD

Crystallographic analyses of the tested catalysts were performed by means of in situ X-ray diffraction (XRD) measurements in  $\theta$ – $2\theta$  mode using a Bruker-AXS D8 Discover apparatus with  $\text{Cu K}\alpha$  radiation of wavelength 0.154 nm and a linear detector covering a range of  $20^\circ$  in  $2\theta$  with an angular resolution of approximately  $0.1^\circ$   $2\theta$ . While the minimal capturing time is 0.1 s, a collection time of 10 s was typically used during these experiments.

In materials science, in situ XRD during annealing can be used to study crystallization [37], grain growth [38], crystallographic phase changes [39] or solid-state reactions [40]. Here, we use this technique for studying solid–gas interactions [13,41], i.e. to investigate the evolution of the catalyst structure during temperature programmed reduction or re-oxidation in a flowing gas stream.

The evolution of the catalyst structure during temperature programmed reduction or re-oxidation was investigated by in situ XRD in a flowing gas stream (5 vol%  $\text{H}_2$ /He or 100%  $\text{CO}_2$ ). These in situ experiments were carried out using a home-built reactor chamber with a Kapton foil window for X-ray transmission. A 10 mg sample was evenly spread on a single crystal Si wafer. Interaction between the catalyst material and the Si holder was never observed. The chamber atmosphere was evacuated and flushed before introducing the reducing gas flow. The sample was heated from room temperature to 1073 K at a rate of 20 K/min. In situ XRD during  $\text{CO}_2$ -TPO immediately followed  $\text{H}_2$ -TPR. All samples were monitored with in situ XRD during an isothermal cycling procedure at 873 K. The latter consisted of five 20 min cycles, where 5 min  $\text{H}_2$  reduction was alternated with 5 min  $\text{CO}_2$  re-oxidation, always with 5 min of He purging in between. Temperatures were measured using a K-type thermocouple and corrected afterwards with a calibration curve of the heating device, based on the eutectic systems Au–Si, Al–Si and Ag–Si. Peak positions and widths were determined by means of a Gaussian function, fit to a XRD peak in a chosen range of  $2\theta$  around the peak of interest. The limited angular resolution of the linear detector did not permit accurate determination of crystallite size and unit cell parameters, but did indicate qualitative trends.

### 2.4. Reaction setup and procedures

Activity measurements were carried out at atmospheric pressure in a quartz tube microreactor (i.d. 10 mm), placed in an electric furnace. Typically, 100 mg of sample was packed between quartz wool plugs. The samples were diluted 1:5 with quartz. The temperature of the catalyst bed was measured with K-type thermocouples

touching the outside and inside of the reactor at the position of the catalyst bed. In order to examine the reactivity and stability of these Ni/Ce–Fe materials, experiments were conducted in a fixed-bed reactor at 873–973 K using  $\text{CH}_4$ ,  $\text{CH}_4 + \text{CO}_2$  (1:1) as model fuel.  $\text{CO}_2$  was used as the oxidant for oxidation of the chemical looping material. The total flow rate of the feed gas into the reactor was constantly maintained at 45 mmol/s using Brooks mass flow controllers. The feed and product gas streams were monitored on-line using MS, using argon as internal standard. The instrument was calibrated beforehand for different mixtures of feed and products.  $\text{CH}_4$  was followed at 16 AMU,  $\text{CO}_2$  at 44, 28 and 16 AMU, CO again at 28 AMU,  $\text{H}_2$  at 2 AMU and Ar at 40 AMU. Concentrations were determined taking into account the fragmentation patterns of the compounds. The response of the mass spectrometer detector was regularly verified with calibration gases. A carbon balance with a maximum deviation of 15% was obtained.

The theoretical number of exchangeable oxygen atoms in the oxygen storage material was calculated according to the presence of  $\text{Fe}_2\text{O}_3$  and  $\text{CeO}_2$  using following equations:

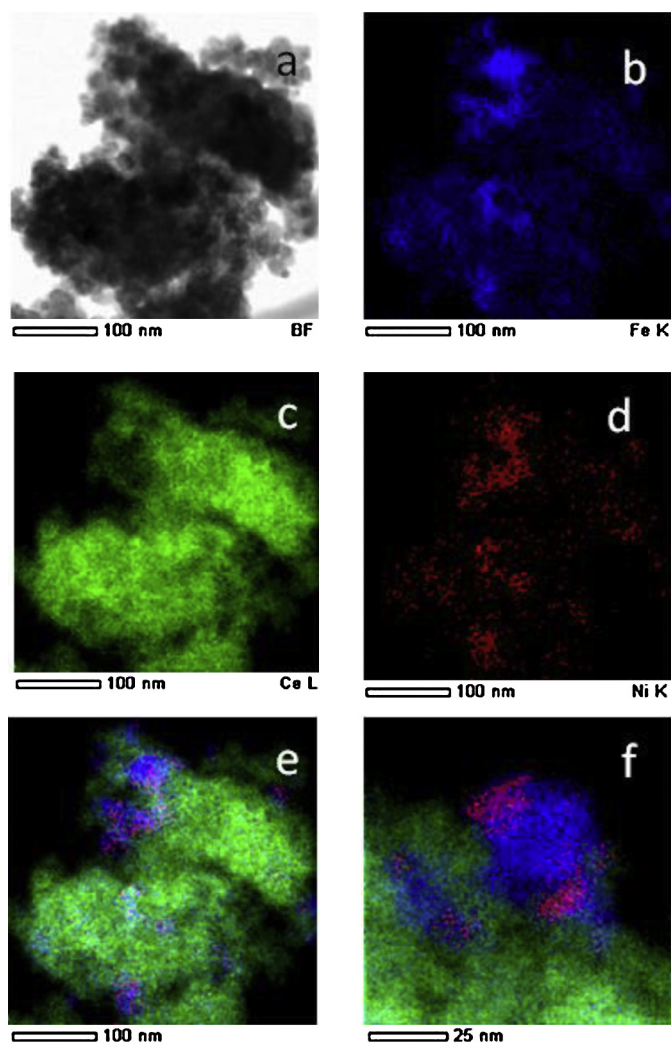
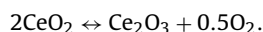
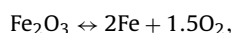


**Fig. 1.** TEM micrograph (a) and EDX element mappings of Fe (b), Ce (c), Ni (d), and the three elements combined (e), with higher magnification of an area with all three elements (f).



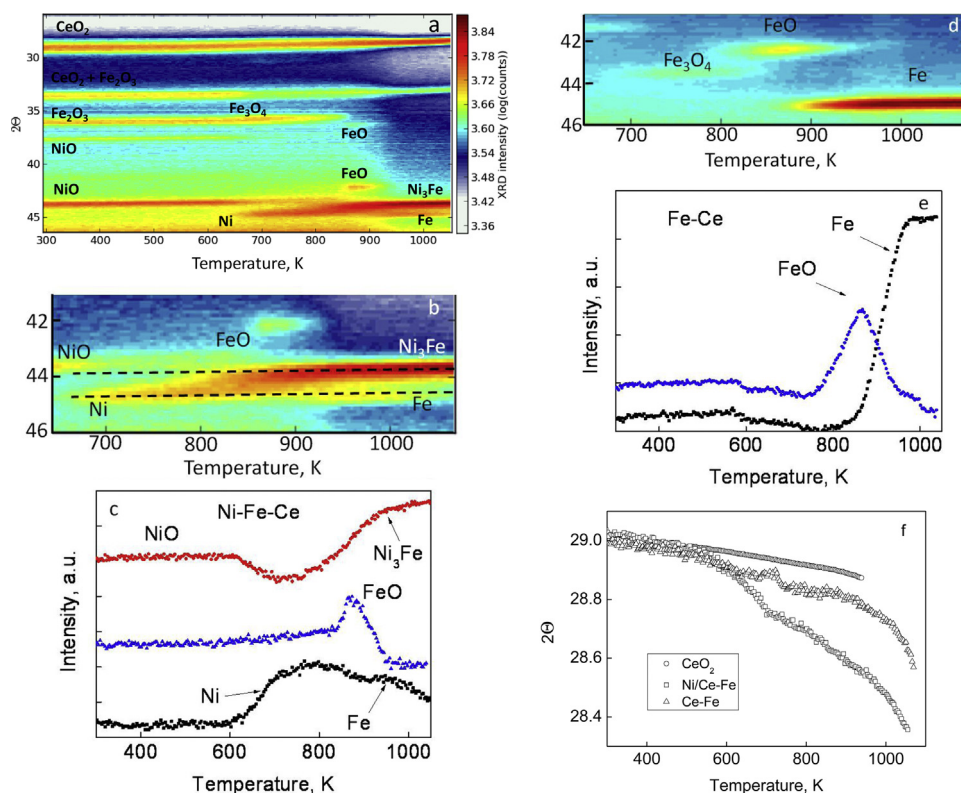


**Fig. 2.** (a) 2D XRD pattern recorded during H<sub>2</sub>-TPR for Ni/Ce-Fe; TPR measuring conditions: 20 K/min; 5% H<sub>2</sub>/He; (b) zoom of (a) to the angular region of Ni<sub>3</sub>Fe alloying; (c) integral intensity variation of (b) for diffractions areas 43.4–44° (NiO), 44.4–44.8° (Ni) and 42–42.5° (FeO); (d) 2D XRD pattern recorded during H<sub>2</sub>-TPR for Ce-Fe; same TPR measuring conditions; (e) integral intensity variation of (d) for diffractions areas 44.4–45.5° (Fe) and 42–42.5° (FeO); (f) CeO<sub>2</sub>(1 1 1) position during H<sub>2</sub>-TPR; variation of CeO<sub>2</sub>(1 1 1) peak position for: ●—pure CeO<sub>2</sub>; ▲—Ce-Fe; ■—Ni/Ce-Fe; same TPR measuring conditions.

The total number of exchangeable oxygen atoms in Fe<sub>2</sub>O<sub>3</sub>–CeO<sub>2</sub> (1:1) was calculated to be 6.2 mol/kg.

### 3. Results and discussion

#### 3.1. Material characterization

TEM images of the Ni/Ce-Fe sample are shown in Fig. 1. The HRTEM micrograph shows crystallites of similar morphology with a size of ~15–20 nm (Fig. 1a). Elemental distribution of the material is indicated using energy-dispersive X-ray spectroscopy (EDX)-STEM mapping. Both Fe (blue) and Ce (green) elements were distributed uniformly in the sample. In contrast, Ni (red) is preferably located close to or on the Fe<sub>2</sub>O<sub>3</sub> particles (Fig. 1b–f).

Time-resolved in situ XRD measurements were performed during H<sub>2</sub>-TPR in order to better understand the transformation of different components of the sample during the reduction process. The result for the Ni/Ce-Fe sample is presented in Fig. 2a. All diffraction peaks exhibit a steady downward shift throughout the TPR due to thermal lattice expansion. During reduction above 650 K, Fe<sub>2</sub>O<sub>3</sub> evolves into Fe<sub>3</sub>O<sub>4</sub> [30.1° (2 2 0), 35.5° (3 1 1) and 43.1° (4 0 0)], into FeO at 850 K [36.0° (1 1 1) and 41.9° (2 0 0)] and finally into Fe [(1 1 0) at 44.7°] above 900 K. At and above 600 K, NiO [43.3° for (2 0 0)] weakens and a Ni peak appears [(1 1 1) at 44.5°]. Between 775 K and 900 K, the Ni peak shifts downward and passes into an alloy peak at a slightly lower angle of ~44° (see zoomed Fig. 2b). The formation of Ni-Fe bimetallic compounds after reduction by hydrogen has been previously described in Ni-Fe samples [31,34,42–45]. In these experiments a full-range XRD scan identified the alloy as Ni<sub>3</sub>Fe (data not shown) (PDF 03-065-3244).

The kinetics of the alloying process are depicted in Fig. 2c as time-dependent integral intensities of the NiO, Ni, FeO, Fe and

Ni<sub>3</sub>Fe diffractions. The intensity of the diffraction at 43.4°–44° corresponding to NiO begins to decrease at 600 K due to reduction into Ni and reaches a minimum at 700 K. At 750 K the intensity increases again because of the Ni<sub>3</sub>Fe alloy diffraction, which steadily gains intensity approaching the highest temperature range. This intensity profile correlates with Ni formation, with diffraction at 44.4°–44.8°. Ni appears around 600 K and reaches a maximum at 775 K. Then, the intensity steadily decreases due to the transformation of Ni into the Ni<sub>3</sub>Fe alloy. Because of overlapping Ni and Fe angular positions, the band at 44.4°–44.8° regains some intensity around 950 K when metallic iron is formed from FeO (Fig. 2c). At higher temperatures, the intensity drops again due to Fe consumption in the Ni<sub>3</sub>Fe alloy formation process.

In order to identify the temperature at which Fe evolves during H<sub>2</sub>-TPR, an additional experiment was made using a Ni-free Ce-Fe sample (Fig. 2d). The kinetics of the reduction process are depicted in Fig. 2e by time-dependent integral intensities of the FeO and Fe diffractions. FeO has a maximum at the same temperature (870 K) as in the case of Ni/Ce-Fe. At the same temperature, the Fe peak begins to appear, near the temperature at which Fe and Ni interact and alloy in the Ni/Ce-Fe sample.

Characteristic peaks associated with crystalline CeO<sub>2</sub> remain visible throughout H<sub>2</sub>-TPR until the final temperature of 1073 K for both samples. Peaks of reduced phase Ce<sub>2</sub>O<sub>3</sub> are never observed, but a possible partial reduction was checked at the position of the CeO<sub>2</sub> (1 1 1) diffraction (Fig. 2f). The position shifts steadily downward at first for both Ce-Fe and Ni/Ce-Fe due to thermal expansion, following the shift for pure CeO<sub>2</sub>. Around 573 K, the onset of an additional drop may be observed for both Ce-Fe samples, lasting until temperatures reach 700 K. This indicates partial reduction of CeO<sub>2</sub> since Ce<sup>3+</sup> is larger than Ce<sup>4+</sup>, which can induce a lattice parameter increase and prompt a downward shift of the

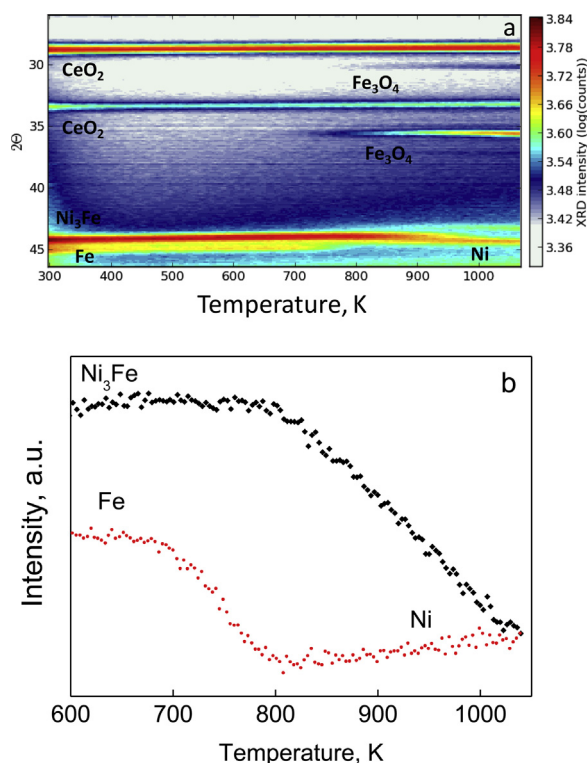


**Fig. 3.** (a) 2D XRD pattern recorded during CO<sub>2</sub>-TPO for Ni/Ce-Fe; TPO measurement conditions: 20 K/min, 100% CO<sub>2</sub>; (b) integrated intensity of selected diffraction peaks vs. temperature.

diffraction peaks [13]. For Ce-Fe, this drop remains limited while for the Ni/Ce-Fe sample it drops further, indicating a larger decrease in lattice parameter and therefore deeper reduction. This indicates that CeO<sub>2</sub> takes part in the oxygen storage capacity of Ce-Fe to some extent by providing lattice oxygen. Bulk reduction of CeO<sub>2</sub> begins around 1023 K [13]. As this temperature lies above the isothermal reaction temperatures used in this study, reduction of CeO<sub>2</sub> will always remain partial.

CO<sub>2</sub>-TPO was performed immediately after cool down following H<sub>2</sub>-TPR (Fig. 3). The oxidation reaction of Fe and CeO<sub>2-x</sub> can proceed through stages reverse to those involved in the reduction. The re-oxidation of Fe to Fe<sub>3</sub>O<sub>4</sub> was observed around 750 K. A weak line lies at 43° from Fe<sub>3</sub>O<sub>4</sub> (4 0 0) as well as possibly reappearing NiO (2 0 0). No intermediate FeO phase is apparent. Formation of FeO strongly depends on reaction temperature and gas composition [13]. The further oxidation of Fe<sub>3</sub>O<sub>4</sub> to Fe<sub>2</sub>O<sub>3</sub> can only be achieved by application of gaseous oxygen [22]. The Ni<sub>3</sub>Fe alloy is stable up to 800 K in a CO<sub>2</sub> atmosphere and then shifts towards 44° around 900 K, where it indicates a remaining Ni contribution. The kinetics of the alloying process are depicted in Fig. 3b by temperature-dependent integral intensities of the Ni<sub>3</sub>Fe and Fe diffractions.

Re-oxidation of Ni to NiO by carbon dioxide is not obvious in Ni/Ce-Fe although a weak NiO contribution might be present at 43° overlapping a Fe<sub>3</sub>O<sub>4</sub> diffraction. However, control experiments over Ni and Ni/CeO<sub>2</sub> samples, which were first reduced during H<sub>2</sub>-TPR and then exposed to CO<sub>2</sub> during TPO (Fig. 4), yielded a similar result. Hence, it is concluded that Ni is not re-oxidized by CO<sub>2</sub>.

In order to examine the stability and evolution of the different phases of Ni/Ce-Fe under different reactive environments, time-resolved in situ XRD measurements during isothermal reduction/oxidation cycling was performed at 873 K. In each re-oxidation, the XRD intensity increases due to enhanced scattering by the CO<sub>2</sub> atmosphere which results in a higher background intensity. A representative set of XRD patterns is plotted in Fig. 5. During the first 3 min the temperature was raised very quickly to the desired value. Patterns are found to repeat during consecutive cycles. Reduction of the sample leads to formation of Fe<sub>3</sub>O<sub>4</sub>, FeO and finally Fe. NiO is reduced and passes into the Ni<sub>3</sub>Fe alloy peak at a slightly lower angle while the Fe peak is appearing. At the end of each reduction step and further during the inert He flow, both Fe and Ni<sub>3</sub>Fe are present. In oxidizing half cycles, the FeO diffractions first gain intensity at the expense of Fe and then quickly give way to Fe<sub>3</sub>O<sub>4</sub> (Fig. 5b), which are maintained until the end of purging. The Ni<sub>3</sub>Fe diffraction does not change significantly during oxidation, since the duration of oxidation is limited. An important point is that this behaviour indicates that the alloyed Fe species remain in a metallic state in the alloy particles during re-oxidation, and their oxidation to Fe oxide is suppressed.

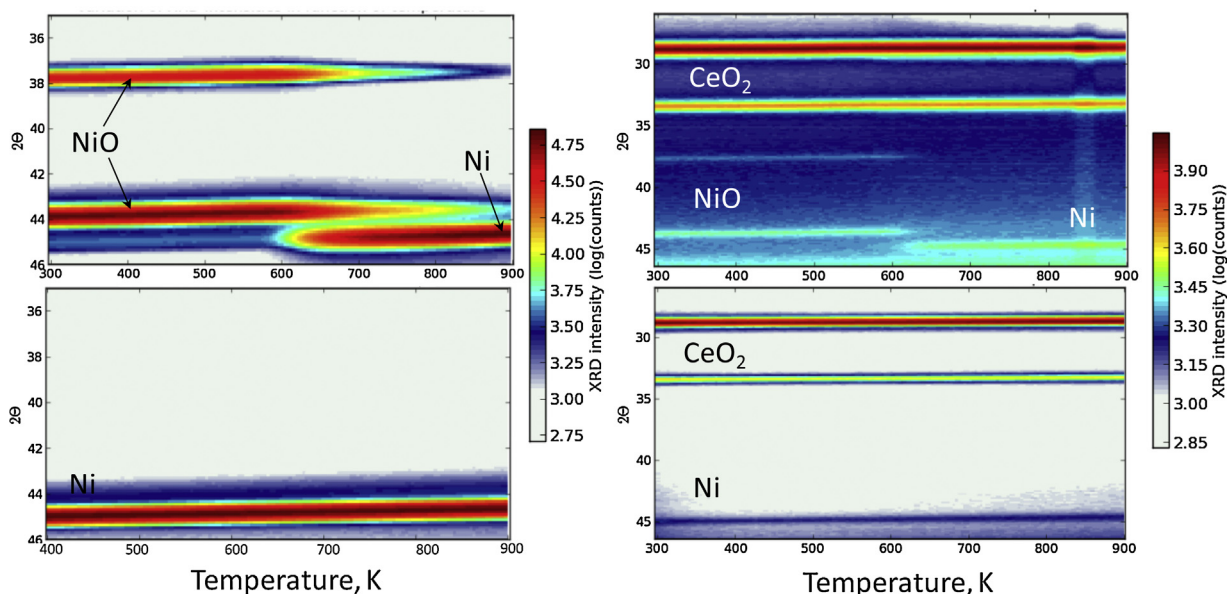


**Fig. 4.** 2D XRD patterns recorded during H<sub>2</sub>-TPR (top panels) on NiO (left panels) and NiO/CeO<sub>2</sub> (right panels) and subsequent CO<sub>2</sub>-TPO (bottom panels); TPR and TPO measurement conditions: 20 K/min heating rate, 5 vol% H<sub>2</sub> in Ar or 100% CO<sub>2</sub>.

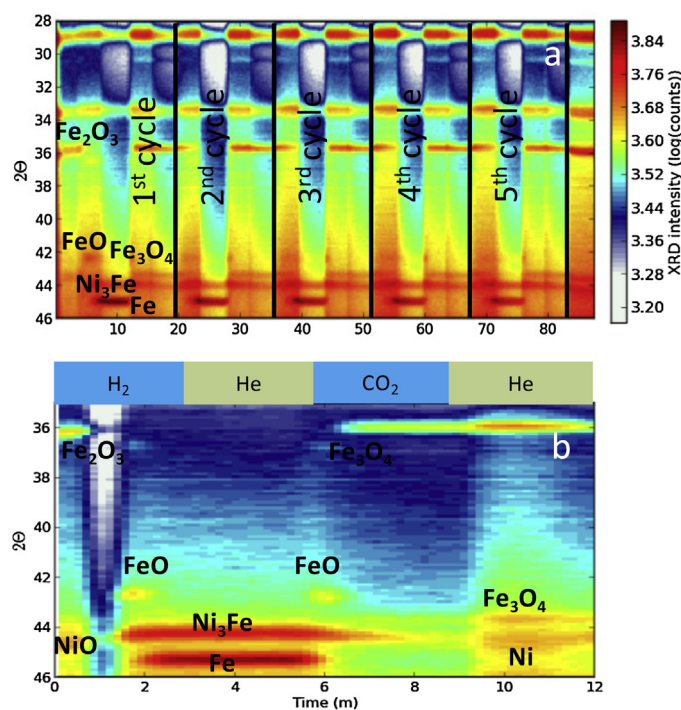


**Fig. 5.** (a) Time-resolved in situ XRD patterns during 5 redox cycles at 873 K, (b) time-resolved in situ XRD patterns during the first redox cycle at 973 K.

However, at an increased cycling temperature (973 K), oxidation leads to separation and transformation of the  $\text{Ni}_3\text{Fe}$  alloy to metallic Ni and  $\text{Fe}_3\text{O}_4$  in all following cycles (Fig. 5b).

### 3.2. Reactivity and stability tests

A series of isothermal reduction/oxidation cycles in a fixed-bed reactor were performed in order to examine the activity and stability of Ni/Ce–Fe materials in catalyst-assisted chemical looping. Inlet and outlet gas compositions were monitored on-line using a mass spectrometer. When a mixture of  $\text{CH}_4$  and  $\text{CO}_2$  (1:1) was fed into the reactor,  $\text{H}_2$ ,  $\text{CO}$ ,  $\text{CO}_2$  and unconverted  $\text{CH}_4$  were detected as reaction products. In Fig. 6a, the space-time yields of methane, carbon oxides and hydrogen are plotted as a function of time on stream at 873 K. During the initial 90 s of the experiment,  $\text{CO}_2$  exhibits a maximum because the CO produced is oxidized by lattice oxygen from the Ce–Fe oxygen storage material. Once this limited quantity of available oxygen is consumed, the space-time yield for  $\text{CO}_2$  is reduced and stabilizes with the other products. The formation of extra  $\text{CO}_2$  in the first part of the reaction indicates that CO contributes to the reduction of  $\text{Fe}_3\text{O}_4$  according to Eq. (5). The space-time yields of CO and  $\text{H}_2$  increase during the initial 90 s of reaction and then reach constant values corresponding only with catalysed dry reforming. The conversion of  $\text{CH}_4$  and  $\text{CO}_2$  amounted to 26 and 30%, respectively.

After purging the reactor with He, carbon dioxide was fed into the reactor for oxidation. Carbon monoxide was produced following contact between the reduced sample and carbon dioxide (Fig. 6b). The CO production reached a maximum at 30 s and then steadily decreased towards zero after 300 s. The feasibility of the catalyst-assistance chemical looping concept very much depends on the possibility to reach a permanent periodic reduction/re-oxidation regime. Therefore, the stability of the different materials was assessed and compared after five cycles. Fig. 7 illustrates the quantity of CO produced during five redox cycles at different temperatures over the Ni/Ce–Fe sample compared to reference Ce–Fe. The reduction/oxidation time for each cycle was 4 and 5 min,

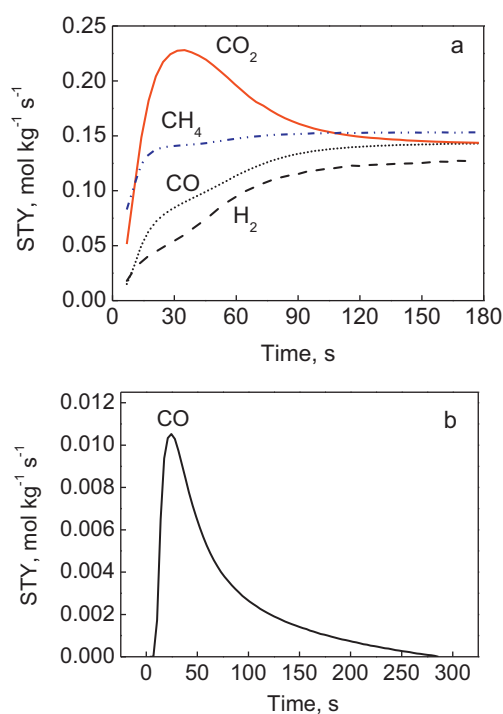


**Fig. 6.** One cycle of reduction and oxidation of the Ni/Ce–Fe sample by  $\text{CH}_4 + \text{CO}_2$  and  $\text{CO}_2$  respectively; (a) catalytic methane dry reforming and oxygen storage material reduction at 873 K: space-time yield vs. time on stream; (b) space-time yield of CO during the re-oxidation phase with  $\text{CO}_2/\text{He}$ .

respectively. Utilization of the bifunctional sample lead to a significant enhancement of CO production compared to the use of Ce–Fe only, e.g.  $\sim 10$ -fold at 923 K. Increasing the reaction temperature over the Ni/Ce–Fe sample lead to even higher CO production. As indicated above, the theoretical oxygen storage capacity of the sample amounts to 6.2 mol/kg in total. This includes 4.7 mol/kg oxygen available in  $\text{Fe}_2\text{O}_3$ , assuming full reduction to Fe, whereas only 1.5 mol/kg oxygen in  $\text{CeO}_2$ , assuming reduction to  $\text{Ce}_2\text{O}_3$ . However, since bulk reduction of ceria only occurs above 1023 K (Fig. 2f) ceria will only reduce partially. Based on the observed CO yield (Fig. 7), the maximum amount of oxygen which was removed from the sample during cycling at 973 K was  $\sim 50\%$  of this theoretical total oxygen storage capacity. This corresponds to deep reduction of iron oxide and only partial reduction of  $\text{CeO}_2$ . Some slight deactivation occurred over the first five cycles. The latter is due to sintering of the iron oxide, not of NiO, as checked from post-cycling XRD and

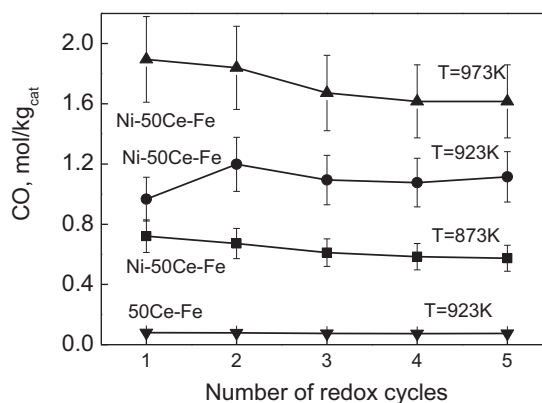


**Fig. 7.** Comparison of CO produced during five cycles at different temperatures  $\blacktriangledown$ —Ce–Fe at 923 K;  $\blacksquare$ —Ni/Ce–Fe at 873 K;  $\bullet$ —Ni/Ce–Fe at 923 K;  $\blacktriangle$ —Ni/Ce–Fe at 973 K. The error bar indicates twice the standard deviation.



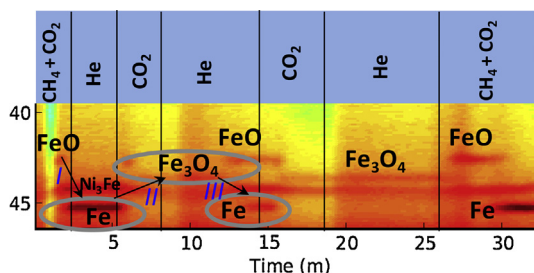


**Fig. 8.** Time-resolved in situ XRD patterns during a reduction/oxidation cycle at 873 K. The arrows indicate the region of Fe reduction (I) and subsequent re-oxidation (II), followed by disappearing  $\text{Fe}_3\text{O}_4$  diffraction and re-appearance of FeO and subsequently Fe in He flow after sample re-oxidation by  $\text{CO}_2$  (III). The sequence of gas environments is indicated at the top.

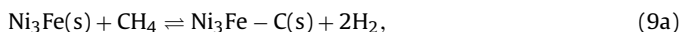
TEM (not shown). This is confirmed by the fact that the conversion of  $\text{CH}_4$  remained the same over consecutive cycles, indicating that the Ni phase holds its catalytic activity.

The yield of carbon monoxide remained close to constant after the fifth redox cycle, which confirmed the stability of the materials' activity. The largest decrease in activity occurs during the first 10 redox cycles followed by slowed activity decay, which is in concurrence with another report in the literature [46].

Side reactions may occur simultaneously with dry reforming depending on the operating temperature and reactant partial pressure [6,47]. These include  $\text{CH}_4$  decomposition (Eq. (7)), where  $\text{CH}_4$  dissociates completely to form solid carbon on the catalyst surface and produce  $\text{H}_2$ , as well as the Boudouard reaction (Eq. (8)), where CO forms surface carbon and  $\text{CO}_2$ .



It was proven worthwhile to look at the  $\text{CO}_2$  re-oxidation process of a reduced Ni/Ce–Fe sample in more detail. A set of XRD patterns is plotted in Fig. 8. During the first minute the temperature was quickly raised to 873 K. At this stable reaction temperature, the intensity of the entire pattern varied as a function of the gas environment. Fe with a characteristic peak at  $45^\circ$  and the  $\text{Ni}_3\text{Fe}$  alloy were formed during the first reduction treatment after 100 s. The Fe peak was converted to FeO and then to  $\text{Fe}_3\text{O}_4$  when  $\text{CO}_2$  was sent into the reactor. The  $\text{Ni}_3\text{Fe}$  alloy phase lost some intensity upon re-oxidation and might even form a small amount of  $\text{NiFe}_2\text{O}_4$  spinel phase. Diffractions for a possible  $\text{NiFe}_2\text{O}_4$  spinel would appear as shoulders to the  $\text{Fe}_3\text{O}_4$  diffractions but go unnoticed due to the low amount of Ni in the sample. The  $\text{Fe}_3\text{O}_4$  phase was stable under  $\text{CO}_2$  flow and after  $\text{CO}_2$  was changed to He. Then, intensity of the  $\text{Fe}_3\text{O}_4$  peaks decreased and eventually completely disappeared, indicating transformation back into FeO and Fe. Simultaneously, the alloy phase regained intensity. A second injection of  $\text{CO}_2$  reconverted FeO and Fe to  $\text{Fe}_3\text{O}_4$ , which then remained stable throughout the entire He flow of 7 min. This suggests that during the reduction step, carbon was formed and accumulated on the catalyst surface (Eqs. (9a) and (9b)) [17,47].



Although at this reaction temperature carbides can be formed,  $\text{Fe}_3\text{C}$  carbide was never observed. This is most likely due to the limited time of reduction in the cycling programme, and to the presence of  $\text{CO}_2$  in the feed.

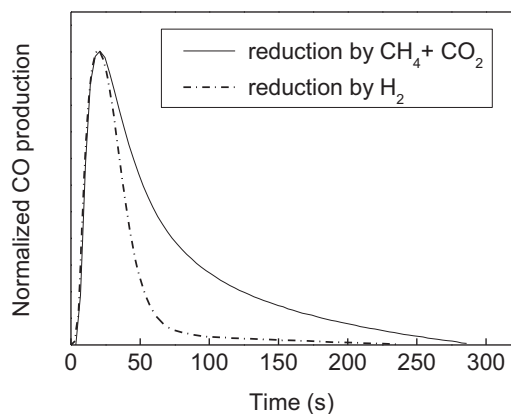


**Fig. 9.** Normalized CO production during the re-oxidation phase with  $\text{CO}_2/\text{He}$ . Dashed line—reduction by 5 vol%  $\text{H}_2$  in He; solid line—reduction by  $\text{CH}_4 + \text{CO}_2$ .

Upon re-oxidation with  $\text{CO}_2$ , iron and partially reduced  $\text{CeO}_2$  are re-oxidized. In turn, the lattice oxygen from the metal oxides oxidizes the surface carbon. In principle, direct oxidation of C by  $\text{CO}_2$  is also possible through the Boudouard reaction [48–50]. However, from the in situ XRD experiment during re-oxidation it is evident that surface carbon oxidation by lattice oxygen (Eq. (10)) takes place equally, since after switching the feed to He, the metal oxide is reduced again (step III in Fig. 8). It is therefore possible to conclude that the first pulse of  $\text{CO}_2$  in Fig. 8 was too short to re-oxidize and remove all C from the catalyst surface. Following this step carbon is further removed by use of lattice oxygen from the Ce–Fe material, giving rise to reduction although no reductive atmosphere is present. Sending a second  $\text{CO}_2$  pulse removed all carbon and re-oxidized Fe back to  $\text{Fe}_3\text{O}_4$ . Comparing the CO produced in the re-oxidation process of the Ni/Ce–Fe sample reduced by  $\text{H}_2$  or by  $\text{CH}_4 + \text{CO}_2$ , the re-oxidation process in the former case occurred significantly faster (see Fig. 9), as the CO production was completed after 70 s. For the sample reduced by  $\text{CH}_4 + \text{CO}_2$ , CO production lasted for 300 s, due to the slow process of surface carbon oxidation.

The overall oxygen capacity of the material determines the duration of a catalytic reaction and therefore the extent of carbon formation on the surface. Usually, formation of coke would be responsible for deactivating the catalytic effect of nickel catalyst particles by fouling of their active sites. This decrease in the number of available active sites could lead to a slowdown in the  $\text{CH}_4$  decomposition and dry reforming rates. Therefore, periodic regeneration of the material is required, as is provided in a chemical looping process, which consists of the two steps of reduction and re-oxidation occurring in a cyclic and discontinuous manner. In addition to refilling the oxygen storage material, the re-oxidation step removes the surface carbon and eventually gives rise to a higher yield of CO compared to the theoretical value corresponding to complete oxidation of Fe to  $\text{Fe}_3\text{O}_4$ .

#### 4. Conclusions

The addition of Ni to  $\text{CeO}_2\text{--Fe}_2\text{O}_3$  had a beneficial effect upon the chemical looping process. In the reduction step, the Ni-based catalyst converts  $\text{CH}_4 + \text{CO}_2$  into a mixture of CO and  $\text{H}_2$ , which both reduce  $\text{CeO}_2\text{--Fe}_2\text{O}_3$ , producing  $\text{CO}_2$  and  $\text{H}_2\text{O}$ . The addition of Ni leads to a deeper reduction of the  $\text{CeO}_2\text{--Fe}_2\text{O}_3$  material. Subsequently,  $\text{CO}_2$  was fed into the reactor for re-oxidation of the reduced material upon which CO was released. The CO yield was proven to be 10 times higher than for  $\text{CeO}_2\text{--Fe}_2\text{O}_3$  without Ni catalyst.

The crystallographic structure of the applied material was examined under  $H_2$  reduction and  $CO_2$  oxidation using time-resolved in situ X-ray diffraction.  $H_2$ -TPR reduced the separate  $Fe_2O_3$  phase to  $Fe_3O_4$ ,  $FeO$  and  $Fe$  while partially reducing  $CeO_2$ .  $NiO$  reduced at 600 K and interaction of  $Ni$  with  $Fe$  lead to formation of a  $Ni_3Fe$  alloy above 800 K. This alloy remained stable during  $CO_2$  re-oxidation to 923 K but completely decomposed into  $Ni$  and  $Fe_3O_4$  above this temperature. Re-oxidation of iron followed a one-step pathway to  $Fe_3O_4$  around 700 K. In redox cycling experiments with alternating  $CH_4 + CO_2$  and  $CO_2$  feeds at 873 K, iron oxide went through consecutive redox cycles while the  $Ni_3Fe$  alloy remained stable in all conditions. The alloy separated into  $Ni$  and  $Fe_3O_4$  only at higher reaction temperatures during oxidation half cycles. However, this separation did not compromise the  $CO$  space-time yield. Methane reforming on the  $Ni/Ce$ - $Fe$  catalyst leads to formation and accumulation of surface carbon. The latter was removed during the  $CO_2$  re-oxidation step by lattice oxygen from  $CeO_2$ - $Fe_3O_4$ . Eventually, the surface carbon gave rise to a higher yield of  $CO$  compared to the theoretical oxygen storage capacity of the  $Ni/Ce$ - $Fe$  material.

## Acknowledgments

This work was supported by the ‘Long Term Structural Methusalem Funding by the Flemish Government’, the Fund for Scientific Research Flanders (FWO, project number 3G004613), and the Interuniversity Attraction Poles Programme, IAP7/5, Belgian State–Belgian Science Policy. We also thank Dr. Vitaliy Bliznuk, Department of Materials Science and Engineering, Ghent University for his support with the HRTEM measurements.

## References

- [1] C. Song, *Catal. Today* 115 (2006) 2–32.
- [2] G.W. Huber, S. Iborra, A. Corma, *Chem. Rev.* 106 (2006) 4044–4098.
- [3] J.-C. Frigon, S.R. Guiot, *Biofuels Bioprod. Biorefin.* 4 (2010) 447–458.
- [4] P. Weiland, *Appl. Microbiol. Biotechnol.* 85 (2010) 849–860.
- [5] S.D. Angeli, G. Monteleone, A. Giaconia, A.A. Lemonidou, *Int. J. Hydrogen Energ.* 39 (2014) 1979–1997.
- [6] D. Pakhare, J. Spivey, *Chem. Soc. Rev.* (2014).
- [7] V. Galvita, K. Sundmacher, *Appl. Catal. A: General* 289 (2005) 121–127.
- [8] M.F. Bleeker, S.R.A. Kersten, H.J. Veringa, *Catal. Today* 127 (2007) 278–290.
- [9] V. Hacker, *J. Power Sources* 118 (2003) 311–314.
- [10] V. Galvita, K. Sundmacher, *Chem. Eng. J.* 134 (2007) 168–174.
- [11] A. Sim, N.W. Cant, D.L. Trimm, *Int. J. Hydrogen Energ.* 35 (2010) 8953–8961.
- [12] R.D. Solunke, G.T. Veser, *Ind. Eng. Chem. Res.* 49, 2010, 11037–11044.
- [13] V.V. Galvita, H. Poelman, V. Bliznuk, C. Detavernier, G.B. Marin, *Ind. Eng. Chem. Res.* 52 (2013) 8416–8426.
- [14] B. Moghtaderi, *Energy Fuels* 26 (2012) 15–40.
- [15] X.P. Dai, J. Li, J.T. Fan, W.S. Wei, J. Xu, *Ind. Eng. Chem. Res.* 51 (2012) 11072–11082.
- [16] S. Bhavsar, M. Najera, G. Veser, *Chem. Eng. Technol.* 35 (2012) 1281–1290.
- [17] J. Plou, P. Duran, J. Herguido, J.A. Pena, *Fuel* 118 (2014) 100–106.
- [18] N. Giannakeas, A. Lea-Langton, V. Dupont, M.V. Twigg, *Appl. Catal. B: Environ.* 126 (2012) 249–257.
- [19] S. Cocchi, M. Mari, F. Cavani, J.-M.M. Millet, *Appl. Catal. B: Environ.* 152–153 (2014) 250–261.
- [20] M. Najera, R. Solunke, T. Gardner, G. Veser, *Chem. Eng. Res. Des.* 89 (2011) 1533–1543.
- [21] P. Heidebrecht, K. Sundmacher, *Chem. Eng. Sci.* 64 (2009) 5057–5065.
- [22] J. Zielinski, I. Zglinicka, L. Znak, Z. Kaszkur, *Appl. Catal. A: General* 381 (2010) 191–196.
- [23] M. Olea, I. Sack, V. Balcaen, G. Marin, H. Poelman, K. Eufinger, R. De Gryse, J.S. Paul, B.F. Sels, P.A. Jacobs (Eds.), *Abstracts of Papers of the American Chemical Society Part 1*, American Chemical Society, 2004, U496–U496.
- [24] V. Galvita, H. Poelman, G. Marin, *Top. Catal.* 54 (2011) 907–913.
- [25] T. Odedairo, J. Chen, Z. Zhu, *Catal. Commun.* 31 (2013) 25–31.
- [26] S. Sokolov, E.V. Kondratenko, M.-M. Pohl, A. Barkschat, U. Rodemerck, *Appl. Catal. B: Environ.* 113–114 (2012) 19–30.
- [27] L. Pino, A. Vita, M. Laganà, V. Recupero, *Appl. Catal. B: Environ.* 148–149 (2014) 91–105.
- [28] W. Chen, G. Zhao, Q. Xue, L. Chen, Y. Lu, *Appl. Catal. B: Environ.* 136–137 (2013) 260–268.
- [29] C.E. Daza, A. Kiennemann, S. Moreno, R. Molina, *Appl. Catal. A: General* 364 (2009) 65–74.
- [30] H.S. Potdar, H.-S. Roh, K.-W. Jun, M. Ji, Z.-W. Liu, *Catal. Lett.* 84 (2002) 95–100.
- [31] L. Wang, D. Li, M. Koike, S. Koso, Y. Nakagawa, Y. Xu, K. Tomishige, *Appl. Catal. A: General* 392 (2011) 248–255.
- [32] A. Sonia, E. Bolshak, D. Montane, *Appl. Catal. A: General* 450 (2013) 261–274.
- [33] M. Sturzenegger, L. D'Souza, R.P.W.J. Struis, S. Stucki, *Fuel* 85 (2006) 1599–1602.
- [34] J. Ashok, S. Kawi, *ACS Catal.* 4 (2014) 289–301.
- [35] P. Scherrer, *Nachr. Ges. Wiss. Göttingen*. 26 (1918) 98–100.
- [36] J.W. Niemantsverdriet, *Spectroscopy in Catalysis*, Wiley, 2007.
- [37] W. Knaepen, C. Detavernier, R.L. Van Meirhaeghe, J. Jordan Sweet, C. Lavoie, *Thin Solid Films* 516 (2008) 4946–4952.
- [38] C. Detavernier, S. Rossnagel, C. Noyan, S. Guha, C. Cabral, C. Lavoie, *J. Appl. Phys.* 94 (2003) 2874–2881.
- [39] G. Rampelberg, M. Schaeckers, K. Martens, Q. Xie, D. Deduytsche, B. De Schutter, N. Blasco, J. Kittl, C. Detavernier, *Appl. Phys. Lett.* 98 (2011).
- [40] S. Gaudet, C. Detavernier, A.J. Kellock, P. Desjardins, C. Lavoie, *J. Vac. Sci. Technol. A* 24 (2006) 474–485.
- [41] V. Galvita, M. Filez, H. Poelman, V. Bliznuk, G. Marin, *Catal. Lett.* 144 (2014) 32–43.
- [42] S.B. Simonsen, D. Chakraborty, I. Chorkendorff, S. Dahl, *Appl. Catal. A: General* 447–448 (2012) 22–31.
- [43] C. Kuhrt, L. Schultz, *J. Appl. Phys.* 73 (1993) 1975–1980.
- [44] X.-z. Jiang, S.A. Stevenson, J.A. Dumesic, *J. Catal.* 91 (1985) 11–24.
- [45] K. Gheisari, S. Javadpour, J.T. Oh, M. Ghaffari, *J. Alloys Compd.* 472 (2009) 416–420.
- [46] V. Galvita, T. Hempel, H. Lorenz, L.K. Rihko-Struckmann, K. Sundmacher, *Ind. Eng. Chem. Res.* 47 (2007) 303–310.
- [47] X.E. Verykios, *Int. J. Hydrogen Energ.* 28 (2003) 1045–1063.
- [48] V. Galvita, L.K. Rihko-Struckmann, K. Sundmacher, *J. Mol. Catal. A: Chem.* 283 (2008) 43–51.
- [49] F.W.A.H. Geurts, A. Sacco Jr., *Carbon* 30 (1992) 415–418.
- [50] M.K. Nikoo, N.A.S. Amin, *Fuel Process. Technol.* 92 (2011) 678–691.